Numerical Study on Rock Breaking Mechanism of Supercritical CO₂ Jet Based on Smoothed Particle Hydrodynamics

Xiaofeng Yang[1, *], Yanhong Li[1], Aiguo Nie[1], Sheng Zhi[2] and Liyuan Liu[3]

Abstract: Supercritical carbon dioxide (Sc-CO$_2$) jet rock breaking is a nonlinear impact dynamics problem involving many factors. Considering the complexity of the physical properties of the Sc-CO$_2$ jet and the mesh distortion problem in dealing with large deformation problems using the finite element method, the smoothed particle hydrodynamics (SPH) method is used to simulate and analyze the rock breaking process by Sc-CO$_2$ jet based on the derivation of the jet velocity-density evolution mathematical model. The results indicate that there exisits an optimal rock breaking temperature by Sc-CO$_2$. The volume and length of the rock fracture increase with the rising of the jet temperature but falls when the jet temperature exceeds 340 K. With more complicated perforation shapes and larger fracture volumes, the Sc-CO$_2$ jet can yield a rock breaking more effectively than water jet, The stress analysis shows that the Sc-CO$_2$ rock fracturing process could be reasonably divided into three stages, namely the fracture accumulation stage, the rapid failure stage, and the breaking stabilization stage. The high diffusivity of Sc-CO$_2$ is identified as the primary cause of the stress fluctuation and W-shaped fracture morphology. The simulated and calculated results are generally in conformity with the published experimental data. This study provides theoretical guidance for further study on Sc-CO$_2$ fracturing mechanism and rock breaking efficiency.

Keywords: Supercritical carbon dioxide jet, rock breaking, SPH, stress distribution, erosion morphology.

1 Introduction

Supercritical carbon dioxide (Sc-CO$_2$) is a special fluid with a gas-like viscosity and a liquid-like density, which facilitate fracture initiation and propagation and improve reservoir permeability compared to ordinary water jets [Middleton, Carey, Currier et al. (2015); Middleton, Viswanathan, Currier et al. (2014); Zhi and Elsworth (2016); Jia, Lu, Elsworth et al. (2018)]. Currently, Sc-CO$_2$ has become a research hotspot in the field of unconventional oil and gas reservoir development for its good prospects in improving

[1] School of Mechanics and Civil Engineering, China University of Mining and Technology, Beijing, 100083, China.

[2] Department of Energy and Mineral Engineering, EMS Energy Institute and G3 Center, Pennsylvania State University, University Park, State College, PA 16802, USA.

[3] School of Civil and Resource Engineering, University of Science & Technology Beijing, Beijing, China.

[*] Corresponding Author: Xiaofeng Yang. Email: xfyang@cumtb.edu.cn.

single well production [Heller and Zoback (2014); Zhi and Elsworth (2014); Zhang, He, Li et al. (2019); Makhanov, Habibi, Dehghanpour et al. (2014); Abedini and Torabi (2014); Zhi, Elsworth and Liu (2019); Zhou, Liu, Jiang et al. (2016); Ranathunga, Perera, Ranjith et al. (2016)]. A larger number of studies [Ishida, Aoyagi, Niwa et al. (2012); Kizaki, Hiroharu, Katsushi et al. (2012); Inui, Ishida, Nagaya et al. (2014)；Liu, Zhu, Wei et al. (2018); Kolle (2002); Zhang, He, Li et al. (2019); Cai, Kang, Wang et al. (2019)] have demonstrated that the a smaller initiation pressures for Sc-CO_2 fracturing, and a more complicated fracture pattern with higher rock-breaking efficiency when using Sc-CO_2 fracturing. The results of Sc-CO_2 rock breaking experiments showed that the low viscosity makes Sc-CO_2 easier to flow into the micropores and microcracks, causing the rock damage via shear and tensile failure [Wang, Li, Tian et al. (2015); Chen, Nagaya and Ishida (2015)]. The current Sc-CO_2 rock breaking mechanism studies have been investigated by analysis of experimental macroscopic morphology, while many effects such as fluid-solid coupling effect, microscopic failure, and particle trajectory have not been studied yet.

Considering phase transition of Sc-CO_2 and its special physical properties, it is relatively difficult to conclude the influence of Sc-CO_2 physical properties on the rock breaking by experiments alone. Li et al. [Li, Feng, Han et al. (2016)] studied the fracturing initiation pressure of the liquid CO_2, water and N_2, and derived the calculation formula of the initiation pressure for cylindrical shale. Lu et al. [Lu, Ao, Tang et al. (2016)] established the adsorption equation for the rock volume changing and derived the mathematical model of Sc-CO_2 fracturing volume expansion in shale. Based on the improved SIMPLE segmentation algorithm, Zhou et al. [Zhou, Lu, Tang et al. (2017)] established a numerical model of the impacting flow field of Sc-CO_2 in the shaft bottom, and obtained the pressure, temperature and physical parameters of the Sc-CO_2 flow field. The numerical simulation method of computational fluid dynamics was also applied to the study of the Sc-CO_2 flow field characteristics, revealing the impacts of the velocity and pressure on the Sc-CO_2 flow field [He, Li, Wang et al. (2016); Wang, Li, Tian et al. (2015)]. However, the recent simulation studies only focused on the characteristics of the post-flow field of supercritical carbon dioxide jet. Due to the complexity of the coupling fluid-solid effect between the jet and rock, few coupling simulations and analyses were conducted on Sc-CO_2 rock fracturing.

Ni et al. [Ni, Wang and Zhang (2005)] used the finite element method to simulate the rock breaking process of the high pressure water jet, and studied the influence of the water jet parameters on rock breaking effect. Sun et al. [Sun, Wang, Yu et al. (2005); Chen, Li, Gao et al. (2015)] studied the impacts of the water jet parameters and rock properties on the rock fracturing efficiency, based on nonlinear finite element method and Hoffman failure criterion. Liu et al. [Liu and Si (2011); Si, Xie and Yang (2011); Xiong, Lv and He (2017)] used the ALE coupled finite element method to simulate and analyze the impacts of the water jet parameters on the internal damage of rock. However, the main limitation of the traditional finite element method is that the mesh distortion reduces the accuracy of the calculation when dealing with a large deformation in the Lagrange method. The Smooth Particle Fluid Dynamics (SPH) algorithm is a novel meshless particle algorithm and could effectively cope with the large deformation and stress and

strain localization without need for finite element mesh. Liu et al. [Liu, Liu and Ji (2015)] used the SPH method to establish a numerical model of the rock breaking by the water jet, and studied impact pressure and rock breaking efficiency at different diameters and speeds of the water jet. Das et al. [Das and Cleary (2010)] used the SPH method to simulate the damage and the fracture of rock by water jet, and verified the ability of SPH method to predict rock fracture comparing with the experimental results. Hedayati et al. [Hedayati and Vahedi (2017)] investigated the penetration in ceramic/aluminum targets using SPH method, and confirmed the target efficiency would be enhanced by increasing the ceramic thickness and decrease of aluminum thickness. Fan et al. [Fan and Li (2017)] couplinged the state-based Peridynamics model with a modifed SPH model, which successfully achieved the large scale simulation of explosive fragmentation of soil up to fve million particles. However, there is still limited literature on the analysis of the Sc-CO_2 rock breaking process by the SPH method.

Based on the derivation of Sc-CO_2 dynamic evolution equation, the Sc-CO_2 rock breaking simulation model is established with SPH algorithm to study the internal stress and damage of the rock. Thus, the rock breaking mechanism by Sc-CO_2 jet is revealed.

2 Physical model of Sc-CO2

2.1 Jet speed

A common cylindrical nozzle is used in the model, and the Sc-CO_2 jet is regarded as the adiabatic friction tube flow [Chen, Cai, Deng et al. (2000)]. The fluid micro-element satisfies the mass conservation equation along the nozzle axis:

$$d(\rho u S) = 0 \tag{1}$$

where ρ is the fluid density, u is the fluid flow velocity, S is the Nozzle cross-sectional area. Ignoring the heat exchange between the fluid and the outside, the fluid micro-element satisfies the one-dimensional steady adiabatic flow energy conservation equation [Tong, Kong and Deng (2012)]:

$$d\left(H + \frac{u^2}{2}\right) = 0 \tag{2}$$

where H is the fluid enthalpy. The fluid satisfies the momentum conservation equation considering friction which is given by:

$$\frac{dp}{\rho} = -u du - \frac{2f u^2}{d} dx \tag{3}$$

where p is the fluid pressure, d is the nozzle diameter; f is the carbon dioxide flow friction coefficient calculated as [Wang, Sun, Wang et al. (2014)]:

$$\frac{1}{\sqrt{f}} = -2.34 \, lg \left\{ \frac{\varepsilon}{1.72d} - \frac{9.26}{Re} lg \left[\left(\frac{\varepsilon}{29.36d} \right)^{0.95} + \left(\frac{18.35}{Re} \right)^{1.108} \right] \right\} \tag{4}$$

where ε is the inwall roughness of the nozzle, d is the nozzle diameter, ρ is the fluid density, Re is the Reynolds number calculated as $Re = \frac{u d \rho}{\mu}$, μ is the hydrodynamic viscosity could be calculated by the Vesovic-Wakeham model [Vesovic, Wakeham and Olchowy (1990)].

For the slow changing of the horizontal flow velocity (du $\approx$ 0) in any micro-element, then Eqs. (2) and (3) could be simplified as:

$$dH = 0 \tag{5}$$

$$\frac{dp}{\rho} = -\frac{2fu^2}{d}dx \tag{6}$$

The physical properties of carbon dioxide are solved by the carbon dioxide equations given by Span et al. [Span and Wagner (1996)]:

$$p(\delta, \tau) = \rho RT(1 + \delta\phi_\delta^r) \tag{7}$$

$$\frac{C^2(\delta,\tau)}{RT} = 1 + 2\delta\phi_\delta^r + \delta^2\phi_{\delta\delta}^r - \frac{(1+\delta\phi_\delta^r-\delta\tau\phi_{\delta\delta}^r)^2}{\tau^2(\phi_{\tau\tau}^0+\phi_{\tau\tau}^r)} \tag{8}$$

where C is the carbon dioxide sound velocity; δ is the conversion density, calculated as $\delta = {\rho_c}/{\rho}$, ρ_c is the critical density of carbon dioxide, τ is the inverse conversion temperature, T is the temperature of carbon dioxide, R is the gas constant of carbon dioxide; ϕ^0, ϕ^r, ϕ_δ^r, ϕ_τ^0 and ϕ_τ^r are the dimensionless Helmholtz free energy function and its partial derivatives.

Therefore, the sound velocity of the inlet flow velocity C_1 could be calculated by Eqs. (7) and (8), then the inlet flow velocity is calculated as:

$$u_1 = C_1 M_1 \tag{9}$$

where M_1 is Mach number. According to the conservation condition at the cylindrical section of the nozzle, the flow velocity of the node i could be obtained by the Eqs. (3), (5), (6) and (9):

$$u_i = \frac{\rho_{i-1}u_{i-1}}{\rho_i} \tag{10}$$

where the p_i is the pressure of the node i.

2.2 Jet density

The density ρ is dynamic in the Sc-CO$_2$ velocity model, and it could be solved by the P-R equations as [Peng and Robinson (1976)]:

$$P = \frac{RT}{V-b} - \frac{a}{V(V+b)+b(V-b)} \tag{11}$$

$$b = \frac{0.08664RT_c}{P_c} \tag{12}$$

$$a = [1 + (0.48 + 1.574\omega - 0.176\omega^2)(1 - T_c^{0.5})]^2 \tag{13}$$

where P is the fluid pressure, R is the gas constant, T is the absolute temperature, and V is the molar volume of gas; T_c is the critical temperature and P_c is the critical pressure, ω is the eccentric factor. For supercritical carbon dioxide, $T_c = 304.2$ k，P_c=7.376 MPa，ω=0.225, and the P-R equation of Sc-CO$_2$ could be obtained by Eqs. (11)-(13):

$$PV^3 + (26.667P - 8.314T)V^2 - (2133.39P + 443.42T - \alpha)V + 18963.6P +$$
$$5912.326T - 26.667 = 0 \tag{14}$$

So the molar volume of carbon dioxide can be obtained by the Eq. (14), and the density could be calculated according to the molar volume as:

$$\rho = \frac{V}{22.4L/mol} \tag{15}$$

3 Numerical methodology

3.1 SPH algorithm

The SPH method bases on the difference algorithm theory, whose particle approximation function is defined as [Lin, Lu, Tang et al. (2014); Libersky and Petschek (1993)]:

$$\Pi^l f(x) = \int f(x)W(x - y, \; l)dy \tag{16}$$

where W is the kernel function defined by the auxiliary function θ as:

$$W(x, l) = \frac{1}{l(x)^n}\theta(x) \tag{17}$$

where n is the spatial dimension and l is the smooth length. Cubic B-spline function is commonly used as the smooth kernel function in SPH which is summarized as:

$$\theta(e) = K \times \begin{cases} 1 - \frac{3}{2}u^2 + \frac{3}{4}u^3 & |e| \leq 1 \\ \frac{1}{4}(2 - u)^3 & 1 \leq |e| \leq 2 \\ 0 & 2 \leq |e| \end{cases} \tag{18}$$

where K is a normalized constant determined by the spatial dimension, $e = \frac{x-y}{l}$.

The Lagrange function for particle motion is stated as:

$$x_j = x_j(x_i, t) \tag{19}$$

where x_i is the coordinates of the particle at the initial moment, and x_j is the coordinates of the particle at time t. The particle motion position equation is:

$$\frac{dx_i}{dt} = v_i \tag{20}$$

where v_i is the velocity of the particle.

The mass conservation equation is:

$$\frac{d\rho(x_i)}{dt} = \sum_{j=1}^{N} m_j \left(v(x_j) - v(x_i)\right) \nabla_i w_{ij} \tag{21}$$

The momentum conservation equation is:

$$\frac{dv(x_i)}{dt} = \sum_{j=1}^{N} m_j \left[\frac{\sigma^{\alpha\beta}(x_j)}{\rho_i^2} - \frac{\sigma^{\alpha\beta}(x_i)}{\rho_j^2} + \Pi_{ij}\right] W_{ij,\beta} \tag{22}$$

The energy conservation equation is:

$$\frac{dE(x_i)}{dt} = -\sum_{j=1}^{N} m_j \left(v(x_j) - v(x_i)\right) \times \left[\frac{\sigma^{\alpha\beta}(x_i)}{\rho_i^2} + \frac{1}{2}\Pi_i\right] W_{ij,\beta} + H_i \tag{23}$$

where $\rho(x_i)$ is the density of the particle, m_j is the quality of the particle, $\sigma^{\alpha\beta}$ is the stress tensor, $v(x_i)$ is the speed of the particle, $E(x_i)$ is the internal energy per unit mass of the particle, Π is a viscous force, W is kernel function. H_i is the enthalpy of the particle.

3.2 Materials and models

The constitutive equation of the Sc-CO$_2$ jet is described by the NULL model in the LS-DYNA material library. And the compressible fluid state of the high-speed impact process is described by the Gruneisen equation as:

$$p = \frac{\rho_0 c^2 \mu \left[1 + \left(1 - \frac{\gamma_0}{2}\right)v - \frac{z}{2}\mu^2\right]}{\left[1 - (s_1 - 1)\mu - s_2\frac{\mu^2}{\mu+1} - s_3\frac{\mu^3}{(\mu+1)^2}\right]} + (\gamma_0 + z\mu)E \tag{24}$$

when the material is stretched, p could be expressed as:

$$p = \rho_0 c^2 \mu + (\gamma_0 + z\mu)E \tag{25}$$

where c is the stress wave velocity, μ is the particle velocity, ϑ_p is the intercept of the curve of c and μ_s; S_1, S_2, S_3 are constants, γ_0 is the Gruneisen coefficient, and z is the first order volume correction factor of γ_0. The parameters of the Sc-CO$_2$ jet [Wang (2013)] are shown in Tab. 1.

Table 1: Physical and mechanical parameters of Sc-CO$_2$ jet

$\rho/(\text{g.cm}^3)$	$\mu/(\text{Pa.}\mu\text{s})$	$C/(\text{cm.}\mu\text{s}^{-1})$	S_1	S_2	S_3	γ_0	a
1.112	0.0015	0.136	2.56	1.986	0.2268	0.11	0

The H-J-C model is used to describe the constitutive relationship of rock with large deformation and high strain rate. The equivalent stress σ^* could be calculated as follows [Polanco, Hopperstad, Borvik et al. (2008)]:

$$\sigma^* = [A(1 - D) + BP^{*N}](1 + F \ln \varepsilon^*) \tag{26}$$

where A is a normalized adhesion strength, B is normalized compression coefficient, P^* is dimensionless pressure, $\dot{\varepsilon}^*$ is dimensionless strain rate, N is the compression enhancement index, F is the strain rate coefficient, and the rock damage factor D is expressed as:

$$D = \sum \frac{\Delta\varepsilon_P + \Delta\mu_P}{\varepsilon_p^f + \mu_p^f} \tag{27}$$

where ε_p^f is the equivalent plastic strain, μ_p^f is the equivalent volume strain, $\Delta\varepsilon_P$ is the increment of the equivalent plastic strain, $\Delta\mu_P$ is the increment of the equivalent volume strain. The rock parameters are shown in Tab. 2.

Table 2: Material parameters of rock

ρ /(g/cm^3)	E_0 /GPa	G /GPa	A	B	S_{Fmax}	N	γ_{Fmin}	T_s /GPa	P_{crush} /GPa	μ_{crush}	P_{lock} /GPa	μ_{lock}	k_1 /GPa	k_2 /GPa	k_3 /GPa
2.44	35.7	14.68	0.79	1.6	7.0	0.61	0.01	0.004	0.016	0.001	0.80	0.1	85	-171	208

Note: E_0 is the elastic modulus, G is the shear modulus, $S_{F_{max}}$ is the normalized maximum strength; $\gamma_{F_{min}}$ is the allowed plastic strain; T_s is the maximum hydrostatic tensile strength; P_{crush}, μ_{crush} are the compressive stress and volumetric strain by uniaxial test, P_{lock} is the locked pressure; k_1, k_2, k_3 are the material parameters.

A three-dimensional model of the Sc-CO$_2$ jet rock breaking was established in LS-DANA (Fig. 1). The radius of Sc-CO$_2$ jet is 4mm, and the symmetry plane is constrained by SPH Symmetry Plane. The rock size is set as 50 mm×50 mm×30 mm. The rock boundary is constrained by a non-reflective boundary condition, while a free boundary is adopted for the fluid.
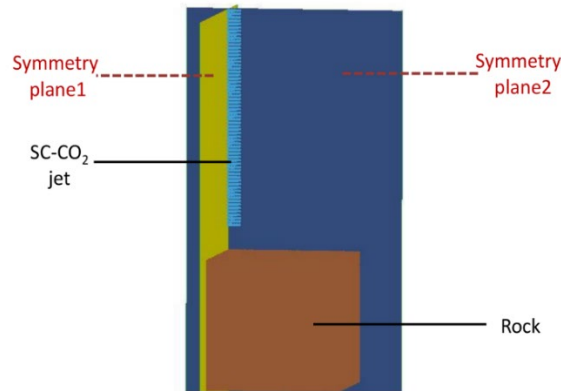

Figure 1: The rock breaking model of Sc-CO$_2$ jet

4 Results and discussion

4.1 Morphology of rock breaking

The simulations of Sc-CO$_2$ and water jet rock breaking are carried out under the conditions of initial temperature 330 k and pressure 60 MPa. The results show that the fractured rock volume by Sc-CO$_2$ jet is greater and more irregular than that by water jet. Moreover, the rock breaking morphology of two kinds of jet is different (Fig. 2): The rock breaking morphology by Sc-CO$_2$ jet presents a "W-shaped" section (Fig. 2(a)), while the rock breaking morphology by water jet is similarly a "V-shaped" section (Fig. 2(b)).
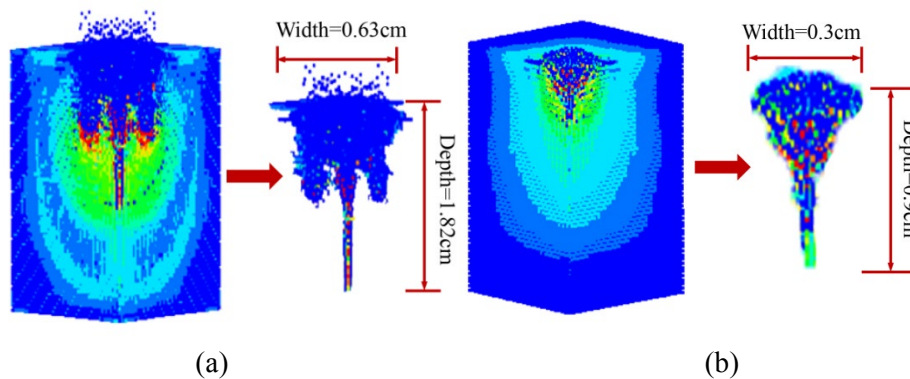

(a)   (b)

Figure 2: The comparison of rock breaking morphology by Sc-CO2 and water jet (Temperature=330 K, Pressure=60 MPa). (a) Rock breaking morphology by Sc-CO$_2$ jet, (b) Rock breaking morphology by water jet

The analysis results also show that the Sc-CO$_2$ jet forms a unique plum blossom shape fracture morphology on the rock surface (Fig. 3), which is consistent with the results of the Sc-CO$_2$ rock fracturing experiment in the literature [Wang, Li, He et al. (2018)].
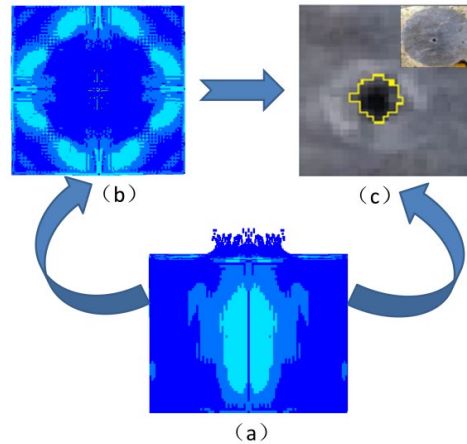

Figure 3: The rock impacting morphology by Sc-CO$_2$ jet. (a) Side view of the rocks impacting by Sc-CO$_2$, (b) Top view of the rocks impacting by Sc-CO$_2$, (c) The experimental photograph of the rocks impacting by Sc-CO$_2$

4.2 Influence of temperature

4.2.1 Fractured volume

The rock breaking processes by Sc-CO$_2$ jet at the temperature of 320 K, 330 K, 340 K, 350 K and 360 K under the pressure of 60 Mpa were simulated and analyzed, and **t**he variation of the rock fractured volume with temperature was thus obtained (Fig. 4). It is shown that the rock fractured volume increases with the rising of the Sc-CO$_2$ jet temperature at the beginning, while it decreases with the increasing temperature after its peak at 340 K. Sc-CO$_2$ jet. Although higher temperature is helpful for the rock breaking [Han, Fang, San-Roman-Alerigi et al. (2019)], too high temperature would reduce the pressure and density of the Sc-CO$_2$ jet, which will reduce the rock breaking ability of the jet impacting. The result indicates that there exists an optimal temperature for the rock fractured volume.
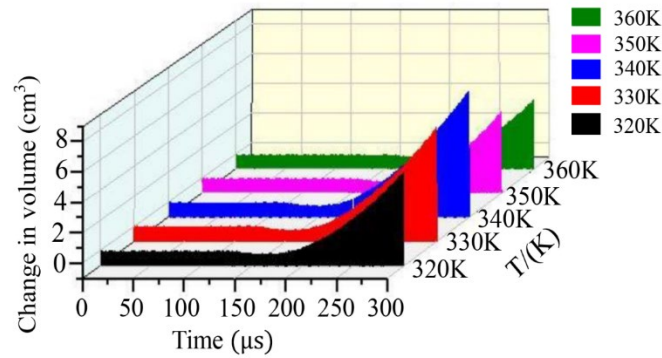
Figure 4: The fractured rock volume at different temperatures

4.2.2 Fractured length

The rock fractured lengths of the Sc-CO_2 jet at the temperatures of 320 K, 330 K, 340 K, 350 K, and 360 K are demonstrated in Fig. 5. It shows that the rock fractured length begins to increase linearly as the temperature increases, and the fractured rock reaches the maximum length at 340 K. After the maximum, the fractured length decreases with the increasing temperature.
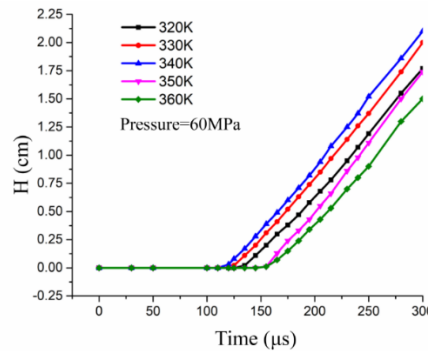

Figure 5: The rock fractured length at different temperatures

4.3 The rock breaking mechanism of Sc-CO_2 jet

4.3.1 Rock breaking speed

The statistical analysis of the cumulative failure unit number with the impact time under the condition of 340 K and 60 MPa is conducted. The rock breaking speed presents a stepped rising trend under the impacting of Sc-CO_2 jet which could be clearly divided into three stages: the fracture accumulation stage, the rapid failure stage and the breaking stabilization stage (Fig. 6).
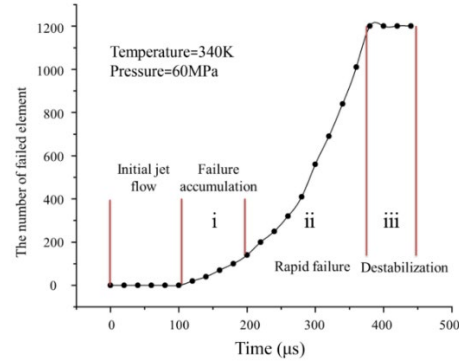
Figure 6: The rock breaking speed by Sc-CO$_2$ jet

In the fracture accumulation stage (i: 100-200 μs), the Sc-CO$_2$ jet begins to impact the rock and the fracturing energy gradually accumulates, the matrix particles on the rock surface begin to loosen and peel off. In the rapid failure stage (ii: 200-400 μs), the rock energy accumulates rapidly, reaching the maximum rock fracture stress, and then the rock begins to break rapidly and massively. Eventually, in the breaking stabilization stage (iii: >400 μs), the impact kinetic energy of the Sc-CO$_2$ jet is reduced, and the rock breakage ceases as due to the lack of sustainable energy supply and the resistance along the path.

4.3.2 The movements of the breaking rock particles

The evolution of rock stress distribution and the fractured morphology by the Sc-CO$_2$ are shown in Fig. 7. Initial stress is formed in the rock when the jet begins to impact on the rock surface (Fig. 7(a)). With the continuous jet impacting, the rock stress rises rapidly and the rock deformmation initiates, showing compression in the normal direction and tensile in the tangential direction. The particles are broken from the rock surface, and the initial perforation is formed as shown in Fig. 7(b). The rock deformation energy around the contact surface is continuously accumulated, causing a rise in the stress and a concentration of the affected area. Then, the impacting stress continues to propagate, as the influence area gradually expands and the particles in axial direction are firstly peeled off (Fig. 7(c)). Due to the impacting of the high-speed Sc-CO$_2$ jet in the axial direction, the axially fractured particles could be expelled upwards along the two sides rather than the axis and conduct shear effects on the surrounding particles (Fig. 7(d)). The expelled fractured particles continue to move upwards, and some of them accumulate in the high-stress areas on both sides, which conduct compression effects on the particles of the side high-stress area. Finally, the particles on both sides of the axis spall and splash on a large scale under the impact stress, shear stress and compressive stress (Figs. 7(e)-7(h)).
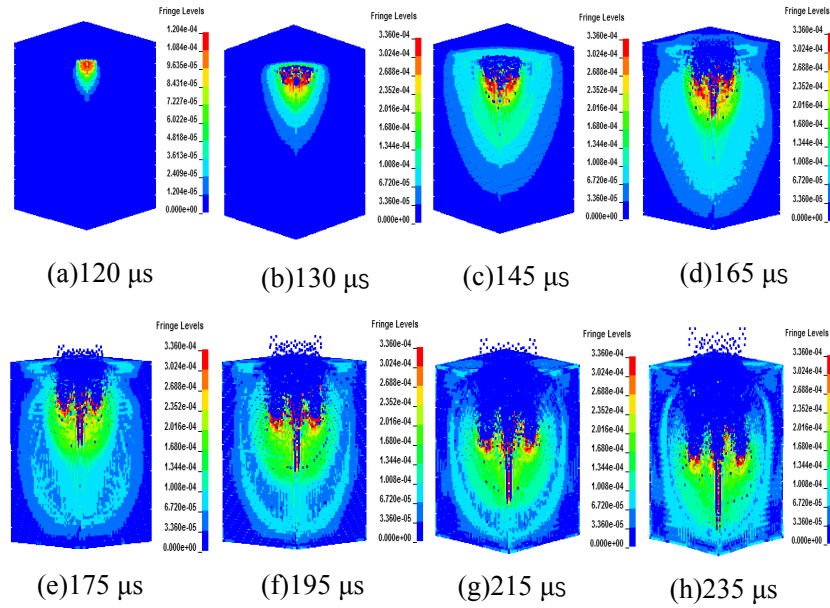
(a)120 μs   (b)130 μs   (c)145 μs   (d)165 μs

(e)175 μs   (f)195 μs   (g)215 μs   (h)235 μs

Figure 7: The evolution of the stress distribution and breaking particles in the rock (Temperature=340 K, Presure=60 MPa)

Rock particles continue to fail and peel off under the impacting of Sc-CO2 jet, resulting in the increasing of the width and depth of the fractured pit, as shown in Fig. 8. The fractured pit begins to form at 110 μs, then the depth of the pit increases linearly. At 240 μs, the depth reached 1.36 cm. The width of the pit increases rapidly during 110 μs to 160 μs, climbing to 0.51 cm. And then the width increases smoothly, the width of the pit reaches to 0.6 cm at 240 μs. The overall simplified motion trajectories of the breaking particles are shown in Fig. 9.
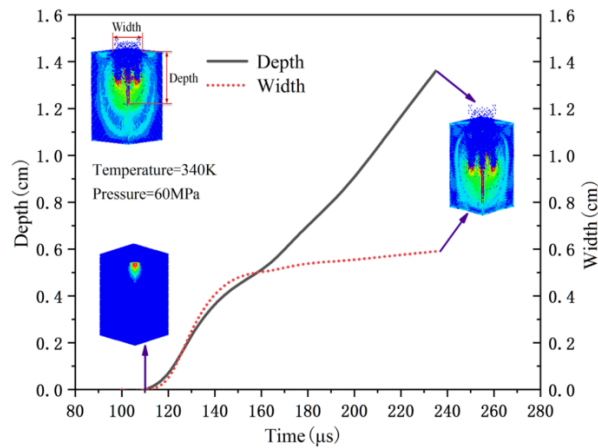

Figure 8: The evolution of the width and depth of the rock breaking by Sc-CO2 jet
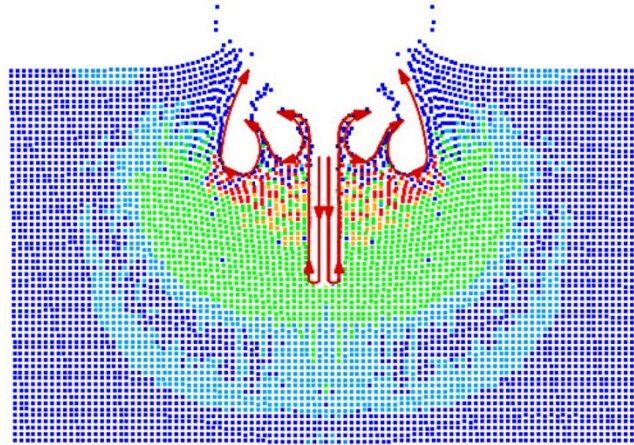
Figure 9: Schematic diagram of the motion trajectory of the breaking rock particles based on the simulation results

4.3.3 Evolution of stress and formation in the rock breaking

Three typical measuring points A (0 cm, 0 cm, 0.5 cm), B (0.5 cm, 0 cm, 0.5 cm), C (0 cm, 4.5 cm, 0.5 cm) on the XOY section was selected to study the stress evolution of rock damage field. The stress variation of each point with time is shown in Fig. 10.
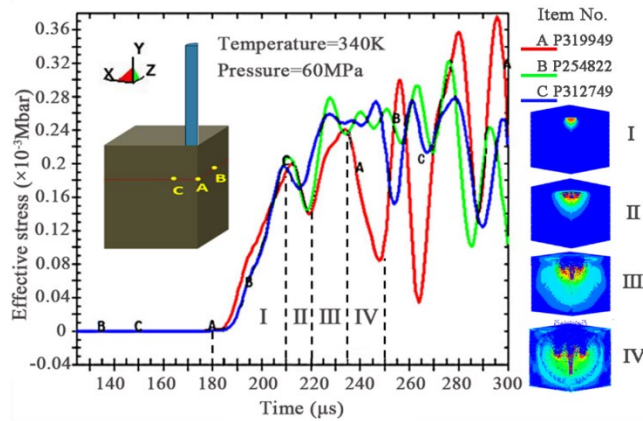

Figure 10: Diagram of the evolution of effective stress in the rock

In the beginning of the jet impacting (180-210 μs), the high-stress core region in the rock begins to appear by Sc-CO_2 jet (Fig. 10(I)). The stress of the three measuring points rises simultaneously, and the breaking energy continues to accumulate until the rock breaks. Subsequently, the earliest rock fracture occurs in the axial direction and forms an erosion pit under the continuous axial stress. Besides, due to the high diffusivity of Sc-CO_2, the rock is also subjected to horizontal stress, and the erosion pit begins to appear horizontal

expansion (Fig. 10(II)). At this time, due to the rock fractures in all directions, the accumulated energy of each point is released, the stress shows a decreasing trend, entering the stress unloading stage (210 μs-220 μs).

As the jet impacting continues, the fractured rock particles are expelled out, and the accumulated energy of the bare rock is continuously replenished. At this time, stress of the measuring point enters the secondary loading stage (220 μs-235 μs), and oblique micro-cracks occur at the top of the rock erosion pit (Fig. 10(III)). Subsequently, the oblique micro-cracks rapidly expand and fracture by the impact and high diffusivity effects of the Sc-CO$_2$ jet, and oblique erosion pits begin to appear in the two wings of the jet, entering into the secondary unloading stage (235 μs-250 μs). In this stage, the axial particles of the same height are firstly fractured and unloaded, causing the particles to loosen and splash at point A. Therefore, the stress of A is lower than B and C. The jet then flows towards the high-stress areas along the wing sides, causing the stress of B and C to rise until the rock particles loosen and splash. Afterwards, the fracure further expands the oblique pit, and finally forms the "W -shape" fracture morphology as shown in Fig.10(IV). Therefore, with the continuously jet impacting, the rock suffers cyclical effects of loading-unloading-secondary loading-secondary unloading, which increases the length and volume of the rock breaking steadily.

5 Conclusions

Based on the derivation of the Sc-CO$_2$ jet velocity-density evolution mathematical model, the Sc-CO$_2$ rock breaking simulation model is developed with SPH algorithm to study the internal stress and damage of the rock. Both morphology of rock breaking and the impact of temperature are throughly examined to define rock breaking mechanism by Sc-CO$_2$ jet. The numerical results are also validated with the reported experimental phenomena. The following conclusions could be drawn:

(1) The velocity-density evolution mathematical model of the Sc-CO$_2$ jet is derived. The numerical model of the Sc-CO$_2$ fracturing is established based on the smoothed particle hydrodynamics (SPH) method, which effectively avoids the mesh distortion in the finite element method. The numerical results are in good consistency with the experimental observations.

(2) The volume and length of the rock fractured by Sc-CO$_2$ jet are obviously greater than that of the water jet. The rock failure morphology is also distinct from the water jet. The fracture morphology of Sc-CO$_2$ jet is "W-shaped", while the sectional surface erosion morphology presents a "plum-shaped".

(3) Jet temperature has a significant influence on the rock breaking by the Sc-CO$_2$ jet. There exists an optimal rock breaking temperature. Under the condition of 60 MPa, both the volume and length of the rock erosion gradually increase with the rising of the temperature of the Sc-CO$_2$ jet. However, it falls when the jet temperature exceeds 340 K, at which the maximum is reached.

(4) The rock breaking speed presents a stepped rising trend under the impacting of Sc-CO$_2$ jet. This trend could be clearly divided into three stages: the fracture accumulation stage, the rapid failure stage, and breaking stabilization stage. The cyclic loading effects on the

rock exist in both axial and horizontal direction simultaneously, resulting in the axial and horizontal rock fracturing and expanding. The high diffusivity of Sc-CO_2 is the main cause of the stress distribution characteristics and special W-shaped rock breaking morphology.

Conflicts of Interest: The authors declare that they have no conflicts of interest to report regarding the present study.

References

Abedini, A.; Torabi, F. (2014): On the CO_2 storage potential of cyclic CO_2 injection process for enhanced oil recovery. *Fuel*, vol. 124, pp. 14-27.

Cai, C.; Kang, Y.; Wang, X.; Hu Y.; Huang, M. et al. (2019): Experimental study on shale fracturing enhancement by using multi-times pulse supercritical carbon dioxide (Sc-CO_2) jet. *Journal of Petroleum Science and Engineering*, vol. 178, pp. 948-963.

Chen, H.; Cai, J.; Deng, X.; Dai, G. (2000): A nozzle flow model of rapid expansion of supercritical solutions process. *Journal of Chemical Engineering of Chinese Universities*, vol. 14, pp. 218-223.

Chen, H.; Li, Z.; Gao, Z.; Sun, Y. (2015): Numerical investigation of rock breaking mechanisms by high pressure water jet. *Procedia Engineering*, vol. 126, pp. 295-299.

Chen, Y.; Nagaya, Y.; Ishida, T. (2015): Observations of fractures induced by hydraulic fracturing in anisotropic granite. *Rock Mechanics and Rock Engineering*, vol. 48, pp. 1455-1461.

Das, R.; Cleary, W. (2010): Effect of rock shapes on brittle fracture using smoothed particle hydrodynamics. *Theoretical and Applied Fracture Mechanics*, vol. 53, pp. 47-60.

Fan, H.; Li, S. (2017): A Peridynamics-SPH modeling and simulation of blast fragmentation of soil under buried explosive loads. *Computer Methods in Applied Mechanics and Engineering*, vol. 318, pp. 349-381.

Han, Y.; Fang, Y.; San-Roman-Alerigi, D. P.; Batarseh, S. I. (2019): Thermal/Mechanical interaction in laser perforation process: numerical-model buildup and parametric study. *SPE Journal*, vol. 24, pp. 2097-2110.

He, Z.; Li, G.; Wang, H.; Shen, Z. (2016): Numerical simulation of the abrasive supercritical carbon dioxide jet: the flow field and the influencing factors. *Journal of Hydrodynamics*, vol. 28, pp. 238-246.

Hedayati, E.; Vahedi, M. (2017): Numerical investigation of penetration in Ceramic/Aluminum targets using Smoothed particle hydrodynamics method and presenting a modified analytical model. *Computer Modeling in Engineering & Sciences*, vol. 113, pp. 295-323.

Heller, R.; Zoback, M. (2014): Adsorption of methane and carbon dioxide on gas shale and pure mineral samples. *Journal of Unconventional Oil and Gas Resources*, vol. 8, pp. 14-24.

Inui, S.; Ishida, T.; Nagaya, Y.; Nara, Y.; Chen, Y. et al. (2014): AE monitoring of hydraulic fracturing experiments in granite blocks using supercritical CO2, water and viscous oil. *48th US Rock Mechanics/Geomechanics Symposium*, American Rock Mechanics Association.

Ishida, T.; Aoyagi, K.; Niwa, T.; Chen, Y.; Murata, S. et al. (2012): Acoustic emission monitoring of hydraulic fracturing laboratory experiment with supercritical and liquid CO$_2$. *Geophysical Research Letters*, vol. 39, pp. 16309.

Jia, Y.; Lu, Y.; Elsworth, D.; Fang, Y.; Tang, J. (2018): Surface characteristics and permeability enhancement of shale fractures due to water and supercritical carbon dioxide fracturing. *Journal of Petroleum Science and Engineering*, vol. 165, pp. 284-297.

Kizaki, A.; Hiroharu, T.; Katsushi, O.; Kiyotoshi, S.; Koji, M. (2012): Hydraulic fracturing in Inada Granite and Ogino Tuff with super critical carbon dioxide. *7th Asian Rock Mechanics Symposium, International Society for Rock Mechanics and Rock Engineering*.

Kolle, J. (2002): Coiled-tubing drilling with supercritical carbon dioxide. *SPE*, PS-CIM 65534: pp. 1-9.

Li, X.; Feng, Z.; Han, G.; Elsworth, D.; Marone, C. et al. (2016): Breakdown pressure and fracture surface morphology of hydraulic fracturing in shale with H$_2$O, CO$_2$ and N$_2$. *Geomechanics and Geophysics for Geo-Energy and Geo-Resources*, vol. 2, pp. 63-76.

Libersky, L.; Petschek, A. (1993): High strain lagrangian hydrodynamics. *Journal of Computational Physics*, vol. 109, pp. 67-75.

Lin, X.; Lu, Y.; Tang, J.; Ao, X.; Zhang, L. (2014): Numerical simulation of abrasive water jet breaking rock with SH-FEM coupling algorithm. *Journal of Vibration and Shock*, vol. 33, pp. 170-176.

Liu, J.; Si, H. (2011): Numerical simulation on damage field of high pressure water jet breaking rock under high ambient pressure. *Journal of Chongqing University*, vol. 34, pp. 40-46.

Liu, L.; Zhu, W.; Wei, C.; Elsworth, D.; Wang, J. (2018): Microcrack-based geomechanical modeling of rock-gas interaction during supercritical CO$_2$ fracturing. *Journal of Petroleum Science and Engineering*, vol. 164, pp. 91-102.

Liu, X.; Liu, S.; Ji, H. (2015): Numerical research on rock breaking performance of water jet based on SPH. *Powder Technology*, vol. 286, pp. 181-192.

Lu, Y.; Ao, X.; Tang, J.; Jia, Y.; Zhang, X. et al. (2016): Swelling of shale in supercritical carbon dioxide. *Journal of Natural Gas Science and Engineering*, vol. 30, pp. 268-275.

Makhanov, K.; Habibi, A.; Dehghanpour, H.; Kuru, E. (2014): Liquid uptake of gas shales: a workflow to estimate water loss during shut-in periods after fracturing operations. *Journal of Unconventional Oil and Gas Resources*, vol. 7, pp. 22-32.

Middleton, R. S.; Carey, J. W.; Currier, R. P.; Hyman, D.; Kang, Q. et al. (2015): Shale gas and non-aqueous fracturing fluids: opportunities and challenges for supercritical CO_2. *Applied Energy*, vol. 147, pp. 500-509.

Middleton, R.; Viswanathan, H.; Currier, R.; Gupta, R. (2014): CO_2 as a fracturing fluid: potential for commercial-scale shale gas production and CO_2 sequestration. *Energy Procedia*, vol. 63, pp. 7780-7784.

Ni, H.; Wang, R.; Zhang, Y. (2005): Numerical simulation study on rock breaking mechanism and process under high pressure water jet. *Applied Mathematics and Mechanics*, vol. 26, pp. 102-105.

Peng, D.; Robinson, D. (1976): A new two-constant equation of state. *Industrial & Engineering Chemistry Fundamentals*, vol. 15, pp. 59-63.

Polanco, M.; Hopperstad, S.; Børvik, T.; Berstad, T. (2008): Numerical predictions of ballistic limits for concrete slabs using a modified version of the HJC concrete model. *International Journal of Impact Engineering*, vol. 35, pp. 290-303.

Ranathunga, S.; Perera, A.; Ranjith, G.; Bui, H. (2016): Super-critical CO_2 saturation-induced mechanical property alterations in low rank coal: an experimental study. *Journal of Supercritical Fluids*, vol. 109, pp. 134-140.

Si, H.; Xie, Y.; Yang, C. (2011): A brasive water jet under the action of rock damage field of numerical simulation. *Rock and Soil Mechanics*, vol. 32, pp. 935-940.

Span, R.; Wagner, W. (1996): A new equation of state for CO_2 covering the fluid region from the triple point temperature to 1100 K at pressure up to 800 MPa. *Journal of Physical and Chemical Data*, vol. 25, no. 6, pp. 1509-1596.

Sun, Q.; Wang, Z.; Yu, J.; Zhang, W. (2005): A disquisition on breaking mechanism of high pressure jet impacting on rock. *Rock and Soil Mechanics*, vol. 6, pp. 978-982.

Tong, B.; Kong, X.; Deng, G. (2012): *Gasdynamics*. Higher Education Press, Beijing.

Vesovic, V.; Wakeham, W.; Olchowy, A. (1990): The transport properties of carbon dioxide. *Journal of Physical and Chemical Reference Data*, vol. 19, pp. 763-808.

Wang, H.; Li, G.; He, Z.; Wang, S. (2018): Analysis on the mechanisms of supercritical CO2 fracturing. *Rock and Soil Mech*anics, vol. 39, pp. 91-98.

Wang, H.; Li, G.; Tian, S.; Cheng, Y.; He, Z. et al. (2015): Flow field simulation of supercritical Carbon dioxide jet: comparison and sensitivity analysis. *Journal of Hydrodynamics*, vol. 27, pp. 210-215.

Wang, J. (2013): *Damage Mechanism of Shale Rock Subjected to Supercritical Carbon Dioxide Jet* (*Ph.D. Thesi*s). Chongqing University.

Wang, Z.; Sun, B.; Wang, J.; Hou, L. (2014): Experimental study on the friction coefficient of supercritical carbon dioxide in pipes. *International Journal of Greenhouse Gascontrol*, vol. 25, pp. 151-161.

Xiong, X.; Lv, Y.; He, X. (2017): Research on the impact characteristics of pulsed water jet with SPH-FEM coupling algorithm. *Machine Design and Research*, vol. 2, pp. 151-155.

Zhang, Y.; He, J.; Li, X.; Lin, C. (2019): Experimental study on the supercritical CO$_2$ fracturing of shale considering anisotropic effects. *Journal of Petroleum Science and Engineering*, vol. 173, pp. 932-940.

Zhi, S.; Elsworth, D. (2016): The role of gas desorption on gas outbursts in underground mining of coal. *Geomechanics and Geophysics for Geo-Energy and Geo-Resources*, vol. 2, pp. 151-171.

Zhi, S.; Elsworth, D.; Liu, L. (2019): W-shaped permeability evolution of coal with supercritical CO$_2$ phase transition. *International Journal of Coal Geology*, vol. 211, pp. 103221.

Zhou, J.; Liu, G.; Jiang, Y.; Xian, X.; Liu, Q. et al. (2016): Supercritical carbon dioxide fracturing in shale and the coupled effects on the permeability of fractured shale: an experimental study. *Journal of Natural Gas Science and Engineering*, vol. 36, pp. 369-377.

Zhou, Z.; Lu, Y.; Tang, J.; Zhang, X.; Li, Q. (2017): Numerical simulation of supercritical carbon dioxide jet at well bottom. *Applied Thermal Engineering*, vol. 121, pp. 210-217.